Open celled material structural properties measurement: from morphology to transport properties

Jérôme Vicente, Frederic Topin, Jean-Vincent Daurelle

Materials Transactions, Vol. 47, No. 9 (2006) pp. 2195 to 2202
Special Issue on Porous and Foamed Metals —Fabrication, Characterization, Properties and Applications—

Open Celled Material Structural Properties Measurement: From Morphology To Transport Properties

Jérôme Vicente, Frédéric Topin and Jean-Vincent Daurelle

Ecole Polytech' Marseille - Laboratoire I.U.S.T.I - UMR 6595 - CNRS Université de Provence - Technopôle de Château-Gombert - 5, Rue E. Fermi 13453 Marseille Cedex 13, France

Metallic foams are highly porous materials which present complex structure of three-dimensional open cells. The effective transport properties determination is essential for these widely used new materials. The aim of this work is to develop morphology analysis tools to study the impact of foams structure on physical transport properties. The reconstruction of the solid-pore interface allows the visualization of the 3D data and determination of specific surface and porosity. We present an original method to measure the geometrical tortuosity of a porous media for the two phases. A centerline extraction method allows us to model the solid matrix as a network of linear connected segments. The thermal conductivity of metallic foams is determined by solving energy equation over the solid phase skeleton. Results obtained on a set of nickel foams covering a wide range of pore size are discussed. [doi:10.2320/matertrans.47.2195]

(Received February 28, 2006; Accepted May 29, 2006; Published September 15, 2006)

Keywords: *Metallic foam, measurement, structural characterizations, heat transfer properties*

1. Introduction

Metal foams are a relatively new class of materials with low densities and attractive thermal, mechanical, electrical and acoustic properties.[1)] Solid foams are widely quoted to present a random topology, high open porosity, low relative density and high thermal conductivity of the cell edges, large accessible surface area per unit volume. Their uses and applications have been widening quickly during the last few years. All these characteristics make metal foam heat exchangers efficient, compact and light weight. Moreover, they also promote mixing and have excellent mechanical properties. Metallic foams are nowadays, proposed as heat transfer enhancer for use in numerous applications such as compact heat exchangers, reformers, biphasic cooling systems and spreaders.[2,3)] For example, metal foams have been used as lightweight supporting structure in aerospace applications.[4)] Different types of metal foams are used as a buffer between a stiff structure and a fluctuating temperature field. They are also used in geothermal operations and in petroleum reservoirs.[5)] Ceramic foams are used in advanced burners and heat pipes. Foams have been used in high-power batteries for lightweight cordless electronics, and catalytic field application such as fuel cells systems.[6)] The control of the texture of porous materials used for the optimization of compact and multipurpose heat exchangers (boiler, vapo-reformer...) represents a significant technological stake.

In general, the lack of morphological tools able to characterize the real microstructures of these foams limits the knowledge of pertinent geometrical parameters able to describe the structure of the foams. Thermo-physical and fluid flow properties depend strongly on local morphology of both pore and solid matrix. Local change in the structure could govern the properties (*e.g.* constriction, strut cross section, surface roughness...). Accurate evaluation of these properties becomes critical for various uses. Models widely used for low porosity media are more difficult to apply to high porosity materials. Due to their novelty, peculiar structure and varied manufacturing processes, metal foams are still incompletely characterized. Indeed, the choice of foam optimized for a given application requires correlating the microscopic structure to the transport properties.

Most of the works dealing with foam transport properties are based on arbitrary periodic structures which represent with variable degree the real texture of the foam. Thus, model remains yet only qualitative.[7–9)] Recent observation using X-ray microtomography[10,11)] showed up the feasibility of the 3D reconstruction and basics measurements on X-ray tomography and proves that this technique is suitable for the investigation of the microstructure of foams. Nevertheless, very few works uses real geometry (usually obtained from 3D X-ray tomography) to determine physical properties.[12)] Mechanical behavior response is found to be strongly anisotropic.[13)] To analyze geometry of foams different methods of visualization, segmentation and morphometry are needed.

We develop specific tools, based on X-ray sample tomography, to characterize both pore space and solid matrix as these two phases may have different geometric characteristics that impact on various properties (*e.g.* heat conductivity is linked mainly to matrix structure, flow laws are governed by pore shape). These tools allow segmentation and geometrical measurements (*e.g.* specific area). Segmentation of pores in individualized cells gives access to both porosimetry and morphometry as well as cells orientations. A centerline extraction method allows us to model the solid matrix as a network of linear connected segments. As physical transport phenomena are directly linked to the path line notion, we calculate geodesics in the medium using a technique based on numerical fast marching implementation. We then determine geometrical tortuosity of each phase.

This approach will enable us to proceed to the morphology analysis in correlation with the physical transport properties obtained via numerical simulations or on experimental data using the tomographied samples.[14,15)] We use a set of Recemat Nickel-Chromium (NC) and reinforced Nickel-Chromium (NCX) foam samples (Table 1). We discuss here

Table 1 Samples Description.

Samples (material-ppi range)	sample diameter (mm)	voxel size (μm)	image size	nb images	nb Cells
NC-3743	16	7.46	2048	292	2305
NC-2733	16	7.46	2048	430	1187
NCX-1723	30	29.47	1326	348	1224
NC-1116	30	29.47	1326	291	604

the used methods and present several results illustrating the main capabilities of our morphological tool (Table 2).

2. Polygonal Model

Starting from X-ray images, two options are usually available for viewing the scalar volume datasets; direct volume rendering[16,17] and volume segmentation combined with conventional surface rendering.[18] The direct volume rendering only supply images of the data whiles the volume segmentation open access to measurements.

We use the classic "Marching cubes" algorithm for extracting interface between the phases.[19] This technique creates a polygonal model that approximates the iso-surface embedded in a scalar volume dataset for a particular iso-value. The surface represents all the points within the volume that have the same scalar value. The reconstruction of the dividing surface between solid and pore allows the visualization of the 3D data (Fig. 1).

The polygonal surface is created by examining each cube of eight voxels and defining a set of triangles that approximates the piece of the iso-surface within the space bounded by the eight points. The efficiency of the algorithm is due to the limited number of cases (256) for which a surface cuts a cube. This allows their tabulation and reduces greatly the calculations. Due to the variation of level variations of X-Ray reconstructed images, an optimal threshold (iso-density) based on the density histogram was calculated for each images. These latter are then re-normalized such as a unique level corresponds to a physical density value in the entire volume. The reconstructed surface is made of regular meshes without holes, nor unconnected edges. We ensure that no duplicated surface or edge exists. We then carry out the direct calculation of surfaces and specific volumes of each phase of the foam. We also export the surface meshes of the solid matrix (or poral space) as toward research or commercial CFD codes to simulate the heat and mass transfers in these mediums.

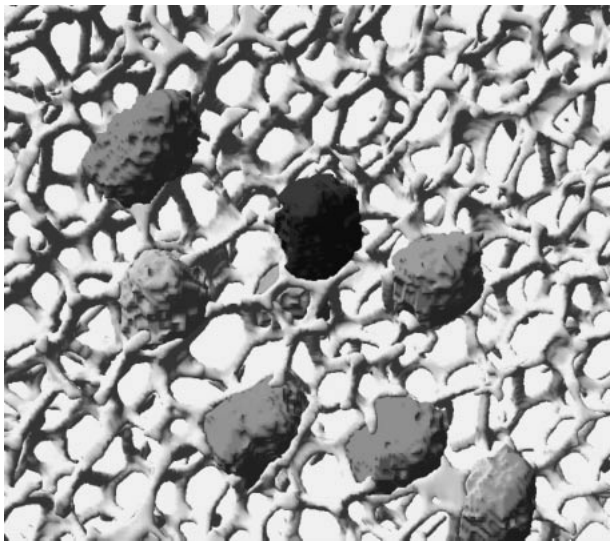

Fig. 1 3D rendering: Solid matrix and segmented pores (Sample NC 27-33).

2.1 Results

Flow laws depend on open porosity. This latter is determined by filling the hollow strut and measuring the remaining porosity. Even the high resolution X-ray images present holes between the macro pore and struts cavities. These holes are either real or created when segmenting the thin walls of struts. To measure both total and open porosity, we apply a 3d closure morphological operation by dilating and eroding the 3d binary images. Eventually, we measure the respective volumes of both pore kinds. The limitation of this technique is the tomography resolution compared to the hollow strut wall thickness. Nevertheless, our results are in good agreement with literature data, and we obtain significant difference between open and total porosity, but it is difficult to quantify uncertainties on these quantities (Table 2). The main objective of this work is to characterize the cells morphology and to extract the solid matrix skeleton. Images resolution has been chosen according to these constrains. In order to precisely quantify porosity a higher resolution is needed since characteristic scale is strut wall thickness.

The specific surface is calculated from the interfacial meshes generated for each sample. The number of triangles constituting the samples meshes is varying from 2 million for the NC-1116 sample up to 5 million for the NC-3743 sample. We found that specific surface varies like the inverse of the mean pore diameter D_p; fitting our data lead to (Fig. 2):

Table 2 Geometrical characterization results.

Samples	Porosity		Specific surface		Aperture diameter		Equivalent ellipsoids			Elongation		Average tortuosity	
	open (%)	total (%)	Sp (m2/m3)	Dp (μm)	pores (μm)	solid (μm)	a (μm)	b (μm)	c (μm)	2a/(b+c)	b/c	solid	pores
NC3743	87.8	88.2	5442	572	428 ± 52	52 ± 6.4	307 ± 33	260 ± 26	214 ± 21	1.29 ± 0.11	1.21 ± 0.1	1.195	1.0057
NC2733	92.2	93.0	3861	831	617 ± 39	39 ± 5.3	453 ± 41	379 ± 30	312 ± 27	1.32 ± 0.12	1.22 ± 0.11	1.208	1.0036
NCX172313	87.3	87.8	1658	1841	1354 ± 192	192 ± 25.8	1052 ± 142	817 ± 92	668 ± 92	1.42 ± 0.17	1.23 ± 0.14	1.178	1.0055
NC111610	89.1	89.7	1296	2452	1792 ± 201	201 ± 28.9	1333 ± 133	1109 ± 89	937 ± 104	1.31 ± 0.13	1.19 ± 0.11	1.179	1.003

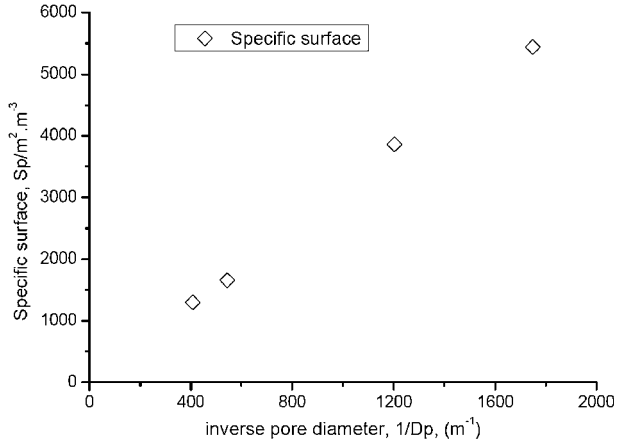

Fig. 2 Specific surface versus pore size.

$$S_p = \frac{3.14}{D_p} \tag{1}$$

This indicates that the tested foams are homothetic.

3. Tortuosity

The tortuosity of a porous medium was for the first time defined by Carman[20] and given, in a particular direction, like the square of the ratio of the average effective distance traversed by the fluid at the Euclidean distance between 2 sections. As we segmented the phases it is interesting to define a geometrical tortuosity for each phase (solid matrix, pores). This tortuosity is defined in Ref. 21), for a couple of points contained in the same phase and connected according to:

$$\tau_g(p_1, p_2) = \left[\frac{L_{\min}(p_1, p_2)}{\|p_1 - p_2\|}\right]^2 \tag{2}$$

with $L_{\min}(p_1, p_2)$, the length of the shortest path in the phase joining p_1 to p_2.

This tortuosity, defined for a couple of points, is not suitable to correlate transport properties to morphology. Indeed, it is the average tortuosity between two surfaces in a direction that govern transport phenomena. We propose a numerical technique to calculate an averaged geometrical tortuosity between two parallel planes in a given direction that fit this empirical definition and thus will be comparable to experimental results.

3.1 Fast marching method

The level set method is a numerical technique for tracking moving interfaces. The related fast marching methods (FMM) which are used for tracking monotonically advancing fronts,[22,23] are computationally attractive. FMM are mainly used for the construction of geodesic on surfaces, or calculation of optimal ways circumventing obstacles.[24] The key advantages of these methods are that they rely on a fixed grid (adapted to discrete 3D images), and handle topological changes in the interface naturally.

A moving interface $\Gamma(t)$ can be formulated as the zero level curve of a scalar-valued function Ψ: $R^3 xR \to R$, where

$$\Gamma(t) = \{x \in \Re^3 : \Psi(x, t) = 0\} \tag{3}$$

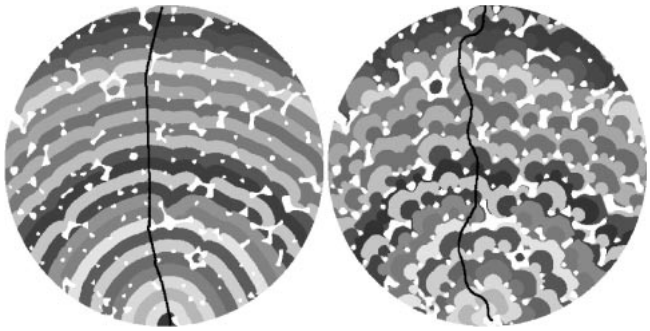

Fig. 3 Geodesic distance map and minimal between 2 points in the pore. Left constant velocity propagation, right distance to solid driven velocity.

Ψ is the crossing time map, a function that gives the time when a moving front crosses the point x. The crossing time is unique if the front is monotonically advancing. Thus, $\Psi^{-1}(0)$ is the initial position of the front and, at any later time t, the front is given by $\Psi^{-1}(t)$. The crossing time map is constructed by solving an equation of the form

$$\|\vec{\nabla}\Psi(x)\| = \frac{1}{F(x)} \tag{4}$$

where $F(x)$ is the front velocity at the point x.

If $F(x) = C^{te}$, then the solution $\Psi(x) = \varphi(x)$ gives the distance from x to the zero contour $\Psi^{-1}(0) = \varphi^{-1}(0)$. The FMM solves this equation by systematically advancing the front by marching outwards from the boundary data. For N nodes, the method has a total operation count of O(N log N). Marching algorithm makes use of an upwind finite differences scheme to compute the value u at a given point $x_{i,j}$ of the grid. We use this method to compute efficiently the distance map, and the minimal path between any pair of point in a given phase. That allows us to determine:

- the geometrical tortuosities of each phases
- An accurate morphological criterion to segment the pore.

To calculate the distance map of every point in the media from the bound we fix the initial position of the front $\Psi^{-1}(0)$ to the frontier points $\Gamma(0) = \{x | x \in \delta\Omega\}$.

3.2 Minimal path extraction

Using the $\Psi(x)$ map over one phase we calculate geodesic joining a given point p_0 to any point p, a 4th order Runge-Kutta method is used to seek the parametric curve $C(t)$ which is the solution of the retropropagation equation:

$$\frac{dC(t)}{dt} = -\vec{\nabla}\Psi(x, t) \text{ with } C(0) = p \tag{5}$$

Using a constant front propagation velocity for the FMM calculation, we obtain the true geodesic path. While a front velocity proportional to the distance of the other phase leads to create an "averaged" path similar to the Carman definition (Fig. 3).

3.3 Results

For each phase, we measure the geometrical tortuosity between two parallel planes situated at the two extremity of the sample. This evaluation is made for two orthogonal

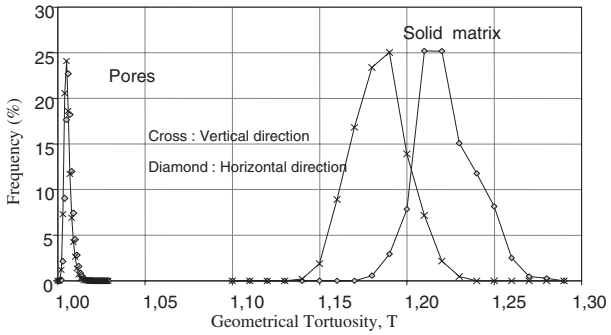

Fig. 4 Tortuosity distribution—left pore, right solid matrix (sample NC 27-33).

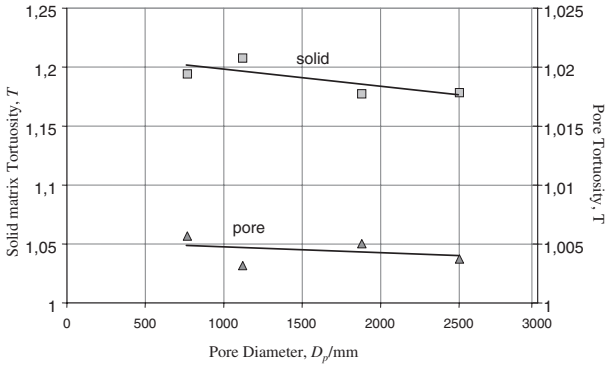

Fig. 5 Tortuosity of both solid and pore phases versus pore size.

direction named horizontal and vertical. These latter are arbitrary and correspond to the initial image orientation. We don't report results on the third direction as there is not enough pores in the thickness of the sample to valuable results. Figure 4 shows the distribution of these tortuosities for each phase and direction. The tortuosity distribution of poral space is very narrow and centered on a low values that indicates a very open texture of pores. On the other hand, the tortuosity distribution of the solid phase is rather large, with an average value of 1.2 very different from the pore tortuosity value. Moreover, the results show clearly that solid tortuosity depends on direction and the solid structure is slightly anisotropic as the effective thermal conductivity (§4.4.2).

Figure 5 shows influence of pore size on tortuosities (average on the two directions). We do not systematically compare tortuosity on each direction because vertical and horizontal directions are arbitrary. Both pore and solid tortuosity values seem to decrease slightly with pore diameter D_p. more work is needed to clarify this point. Tortuosity values are probably correlated to cells shape and orientation. A systematic study is undergoing to evaluate angular variation of tortuosity and to determine principal sample orientation.

4. Segmentation of Pore and Solid Phase

4.1 Aperture diameter

One way to characterize the pore size is to determine the aperture diameters map. The local aperture diameter $Ouv(P)$ is defined at any point P of an object as the diameter of the largest ball included in the object and containing the point P, as proposed by Ref. 25).

$$Ouv(P) = \max\left\{d | B\left(C, \frac{d}{2}\right) \subset O, P \in B\left(C, \frac{d}{2}\right)\right\} \quad (6)$$

The aperture map is then defined as a 3D image of local aperture diameter. This map is constructed by affecting $Ouv(P)$ to each voxel P as shown on Fig. 6. The histogram of this map gives access to the pore size distribution (Fig. 7). Nevertheless, this technique is limited to the evaluation of pore size. No direct information on cells shape could be deduced from these data alone. The pore aperture diameter D_a is the mean diameter of the maximal included sphere distribution.

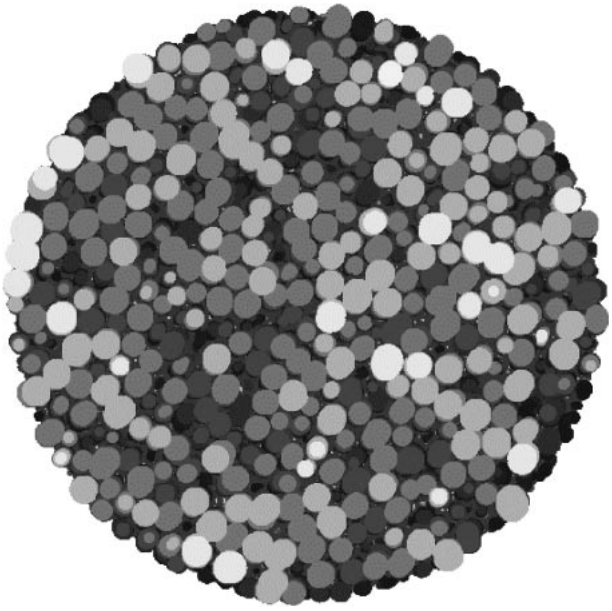

Fig. 6 Aperture map in a cross section (sample NC 27-33).

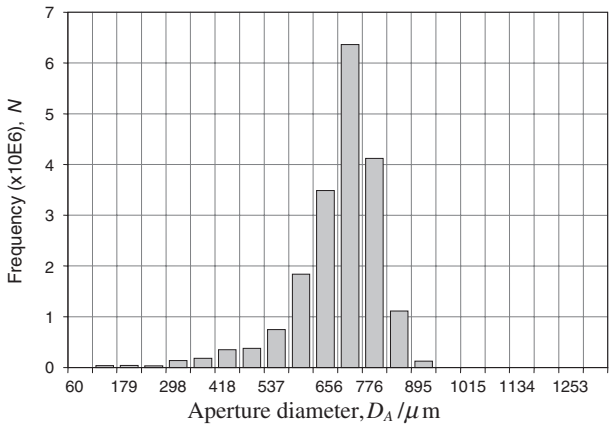

Fig. 7 Pore aperture size diameter distribution (sample NC 27-33).

4.2 Cells segmentation

3D segmentation of the cells is necessary to characterize completely the cells shape (Fig. 1). As the cells are fully open cells it is very difficult to extract them through classical morphological operations such as erosion/dilation processes.

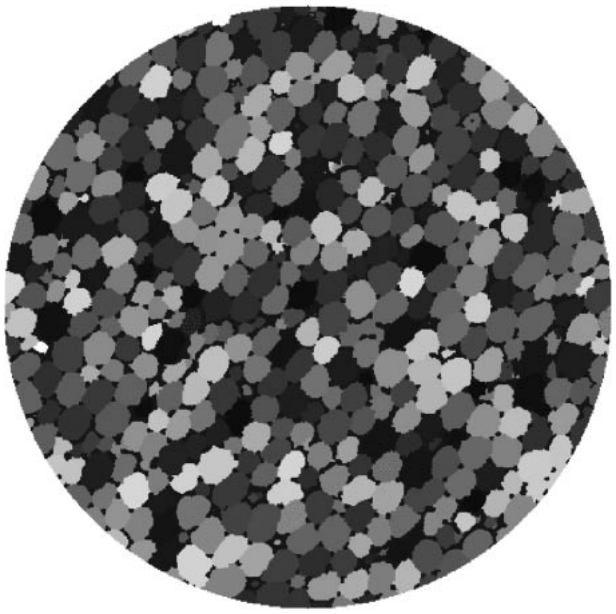

Fig. 8 Cross section of segmented cells (sample NC 27-33).

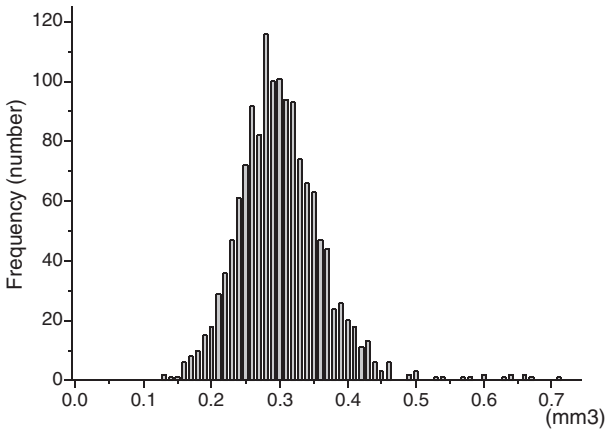

Fig. 9 Segmented cells volume distribution (sample NC 27-33).

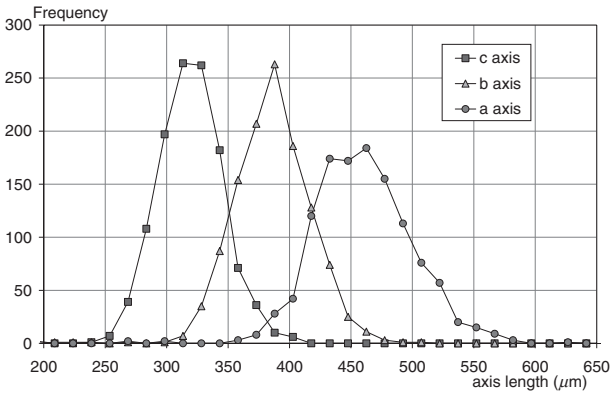

Fig. 10 Half axis length of equivalent ellipsoid distribution. Statistic made from 2000 cells (sample NC 27-33).

We use the watershed transform of the marker distance function[26] in order to individualize and to close the open-celled pores in 3D. This segmentation allows to directly measuring cells morphological parameter (volume, equivalent sphere diameter, surface, aspect ratio...).

Markers, defined as the local extrema of the pores distance map, are identified. Because of shape irregularities of struts and cells, as well as presence of constrictions, more than one minimum exist in each cell, while the method needs one unique marker. The key point of this technique is to eliminate irrelevant markers until obtaining the one corresponding to the "center" of the cell. A first class of "false" markers is easily eliminated using topographic conditions. For example, false markers belonging to the centerline of oblong objects, or markers located near solid voxels, are easily eliminated using a threshold distance between solid or other markers. On the other hand, markers belonging to cells throat are not so easily eliminated as they mark a real geometric structure that have a characteristic size close cells size. We develop an elimination method based on analysis of the markers neighborhood. We study the distribution of minimal distance to solid of points located on a sphere (radius r) centered on the marker. These distributions are different according to the marker types. In the case of throat markers, the distribution is wide and its maximal value is close to the marker distance d_M. On the other hand, in the case of cell markers, the distribution is narrow and maximal value is around $d_M - r$. The watershed transforms permits to associate each cell voxels to a unique marker. Incomplete cells at the sample boundary are eliminated.

A large initial volume containing from 600 up to 2300 cells depending on the sample is analyzed in order to obtain statistically representative results (Table 1). Figure 1 shows a 3D rendering of a foam sample and several segmented cells, and Fig. 8 shows a 2D cross section of a segmented sample.

The volume of each cell is simply determined by counting the cell voxels. For example, the average cell volume of sample NC-2733 is 0.3 mm^3. We define D_p as the diameter of the equivalent volume sphere; the mean value being equal to 831 μm (Fig. 9).

The aperture diameter D_a is systematically smaller than the equivalent volume sphere diameter D_p (Table 2); thus cells are not spherical. Indeed, the foaming process of the polyurethane foam template is affected by gravity, which favors cell elongation in the vertical direction. During the nickel foam manufacturing process, several forces can also modify the cell shape.

4.3 Cells shape and orientations

The 3D inertia matrix of the equivalent ellipsoid is determined for each individualized cell. The 3 principal axes of the ellipsoid are denoted respectively by a, b and c with $c < b < a$. The referential O, x, y, z, is determined by the tomography. The plane Oxy is the image plane, whereas the z direction is the thickness of the sample.

An example of distribution of axis length values is presented on Fig. 10. These three distributions are monomodal and rather narrow. The average value of the three parameter a, b, and c are respectively 453 ± 40.9, 379 ± 30.6 and 312 ± 26.7 μm for NC-2733. The three principal axis values are clearly separated even if the three distributions overlap a little. As expected, the three dimensions of the

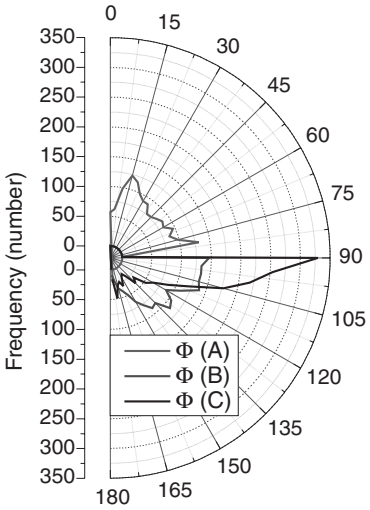

Fig. 11 Polar representation of the orientation of the axes of the equivalent ellipsoid—Elevation (φ) distribution values (sample NC-27-33).

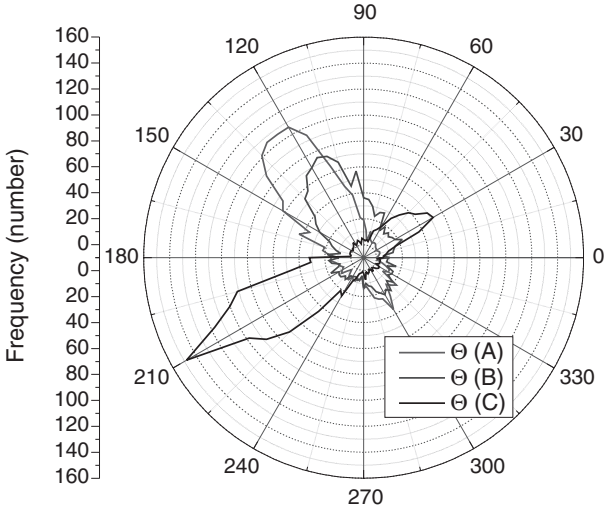

Fig. 12 Polar representation of the orientation of the axes of the equivalent ellipsoid—Azimuth (θ) distribution value (sample NC-27-33).

equivalent ellipsoid are different; the cells are elongated along their principal axis. We can note that the average standard deviation is about 8.5% for the three axes. All the analyzed foams show similar distributions. The mean principal axis values triplet is used as cell descriptor. One can note that the volume of the mean ellipsoid, defined with the three means length of the axes a, b and c, is equal to 0.225 mm^3. The difference with the mean cell volume is due to the fact that the equivalent ellipsoid is by construction the maximal included ellipsoid. The elongations calculated from mean principal axis length are presented in Table 2. These results show clearly that the cells are more elongated along the a-direction. This indicates that the cell deformations due to manufacturing process are produced by independent phenomena of different intensity.

Directions associated with each axis (a, b, and c) are determined using the eigenvectors associated to eigenvalues of the cell 3D inertia matrix. Figures 11, 12 present respectively the polar orientation distribution (elevation φ and azimuth θ) of these axes. We represent the elevation of the a-axis cells into the 0–90° quadrant. The other elevations (b- and c-axes) are plotted into the 90–180° quadrant.

The smallest cell axes (c) are almost horizontal, located into the plane O, x, y, and the distribution is narrow (Fig. 11). A more detailed analysis shows up that the bi-modal shape of a- and b-axes distribution comes from two separate classes of cells. The biggest cells a-axes are rather vertical (near 15°) and the smallest cells a-axes are rather horizontal (75°). We observe a similar effect on the b-axis distribution. The weak difference between b and c mean orientation values shows up that the plane O, b, c is not completely parallel to the sample image plane (O, x, y) as b- and c-axes are, by construction, orthogonal to a-axis.

Figure 12 present the azimuth distribution (orientation of the principal axes into the plane O, x, y). As the sample is a cylinder, the position of the axes O, x and O, y are arbitrary and correspond to the original orientation of the tomographied images. The azimuth distributions show clearly that the three different axes of the cells are oriented along three mean values respectively 125°, 115°, and 200° for the a-, b- and c-axis. Cells are ordered such as axes azimuths stay roughly constant. On the other hand, elevations are more variable, this is probably due to the manufacturing process.

4.4 Solid network

The extraction and the automatic recognition of the structuring elements constitute the base of the geometrical description. Indeed, the identification and the three-dimensional localization of nodes (branching detection), branches and the connectivity table allow us to access the geometrical characteristics. We focus especially the determination of the connectivity of the solid matrix and of the poral space. The network reconstruction open access to statistic treatment of: Segment length, orientation, as well as highlighting preferentially directed planes.

The detection of the junctions of the solid matrix enables us to cut out it in structuring elements (segment, nodes) from which we build an idealized network of linear segments.

4.4.1 Distance ordered homotopic thinning

Skeletons are compact representations that allow mathematical analysis of objects. It must be homotopic, thin and medial in relation to the object it represents. The obtained skeleton is connected, topologically equivalent to the object, centered and thin. We are interested in discrete methods, generally fast and easy to use.

We choose the Distance Ordered Homotopic Thinning[27] (DOHT), which uses a homotopic thinning, this means an iterative deletion of simple points but in the increasing distance map order leading to a centered skeleton.

The skeleton is computed by iteratively peeling off the boundary of the object, layer-by-layer. A point is said simple if its deletion preserves the object topology.[28] If all simple points are removed iteratively the result object is topologically equivalent to the original one, but far simple. A connected component without hole or cavity will be shrunk to a single point. In order to better preserve rotation invariance, we add to this method a directional strategy as proposed by Ref. 27). For each distance, we systematically consider

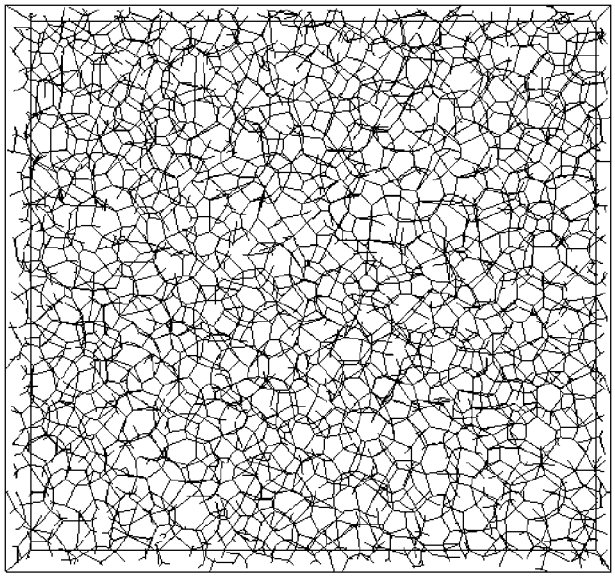

Fig. 13 Idealized solid network (sample NC 27-33).

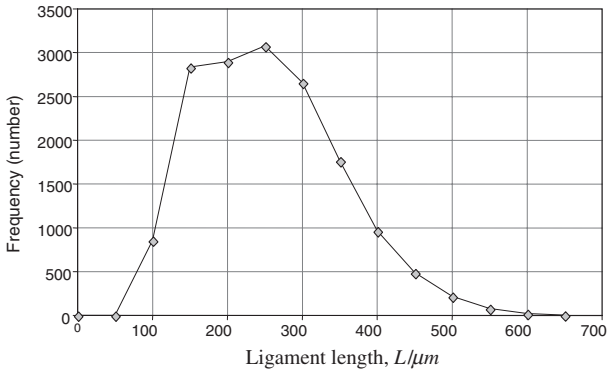

Fig. 14 Struts length distribution. (Sample NC 27-33).

border points, in the following order: east, bottom, west, south then top of the object. We eliminate all the false branches induced by struts irregularities. Such branches are short and connected to a single point.

Oversegmentation often occurs at struts intersection. Morphological operations are then used to remove these small bad struts. This operation take into account different scale of analysis to cleanup these regions. On the cleaned skeleton (Fig. 13) we measure the struts length distribution (Fig. 14). This idealized network is used to determine effective thermal conductivity.

4.4.2 Effective thermal conductivity

Reference 29) provided detailed experimental characterization and numerical modeling of the heat and mass transport properties of highly porous media for solar receivers and porous burners. Several researchers focused on determining the effective thermal conductivity. Reference 30) experimentally determined the effective thermal conductivities of foams made out of aluminum and silicon alloys. Reference 31) presented a semi-empirical model for the combined conduction and convection heat transfer in a thin porous wall. Reference 32) provided experimental measurements and modelling of the thermal and hydraulic aspects of cellular metals subject to transverse airflow. Reference 33) numerically investigated the anisotropy in permeability and effective thermal conductivity on the performance of an aluminum heat sink.

Several authors have implemented prediction models of effective thermal conductivity of foams in purely conductive regime. These models are based on the knowledge of thermophysical properties of the material constituting the metallic matrix, of the fluid within and generally of a structure parameter of the foam (for example ratio between the average sizes of struts and nodes).[7,34,35] All these methods did not take into account the real morphology of the foam but assume an idealized periodic pattern. Besides, measurement were achieved with both stationary[35] and transient methods.[36]

Effective thermal conductivity K_i^{eff} on each direction x, y, z is determined. A cube is cut into the sample RLS and nodes constituted by intersection of each cube face and segments are identified. We impose different temperature on two opposite faces. We calculate the total heat flux Φ_i across the network using the nodal temperature deduced from simple one-dimensional conduction transfer on each segment. On each node p of the network, energy balance is given by

$$\sum_{\substack{j\in\text{Nodes}\\ \text{connected to } p}} \Phi_{pj} = \sum_{\substack{j\in\text{Nodes}\\ \text{connected to } p}} -\frac{k_{solid}}{l_{pj}} S_{pj}(T_j - T_p) = 0 \qquad (7)$$

Where ϕ_{ij}, l_{ij} and S_{ij} are resp. the heat flux and the length and the cross section of the segment. k_{solid} is the solid thermal conductivity, and T_i, T_j are the nodal temperatures.

Eventually, the flux Φ_i is identified with macroscopic conductive heat flux across a homogeneous medium placed in the same conditions and $K_i^{eff} = \frac{\Phi_i e}{\Delta T}$.

Note that we supposed here, that the fluid phase doesn't contribute significantly to the effective conductivity and that radiative transfer between solid surfaces is negligible. The segment section is taken as its mean value deduced from total solid volume and length of the network.

Table 3 shows an example of quantitative results in non dimensional form as well as for the case of an Inconel type solid of thermal conductivity $30\,\mathrm{Wm^{-1}\,K^{-1}}$ which is a typical value for the material constituting our foam sample. The results show a slightly anisotropy of the foam. It is very difficult to evaluate the accuracy of our approach, because we cannot quantify the error of the foam structural schematization and its effect on final conductivity values. Nevertheless, a good agreement with experimental values is obtained.

5. Conclusions

We developed a morphological analysis tool that gives access to quantification of the main structural parameters of metallic foams.

The reconstruction of the dividing surface between solid and pore (made of regular mesh) allows the visualization of the 3D data and the calculation of the specific surface. We also export the surface meshes of the solid matrix (or poral space) toward research or commercial CFD codes to simulate the heat and mass transfers in these mediums. Basic size

Table 3 Effective thermal conductivity. Sample NC-1723.

Total network length	(m)	7.685
Box volume	(m^3)	3.32E-06
Strut section	(m^2)	3.71E-08
Strut equivalent diameter	(μm)	217.5
kx/ksol	(%)	1.99
ky/ksol	(%)	2.33
kz/ksol	(%)	2.79
kx (ksol = 30)	($Wm^{-1} K^{-1}$)	0.60
ky (ksol = 30)	($Wm^{-1} K^{-1}$)	0.70
kz (ksol = 30)	($Wm^{-1} K^{-1}$)	0.84

characterization of pores and struts is obtained using aperture map distribution. Segmentation of pores in individualized cells gives access to detailed morphometry and orientations.

An efficient centerline extraction method gives the skeleton of the solid phase. Identification of nodes, segments, and connectivity of the idealized network modelling the solid matrix has been carried out. Morphology of the solid matrix is thus characterized (struts length, orientations...).

The conductive heat transfers are computed on solid matrix skeleton to determine directional effective conductivities.

Specific experiments are carried out to identify thermal conductivity. Separately, structure morphology measurements are performed for the real medium. The anisotropy of the conductivity is observed and relationship between microstructure and properties is under analysis.

An original method based on numerical fast marching implementation has been developed to independently measure the geometrical tortuosity of the two phases (solid and pore). Tortuosity of poral space is very low compared to solid matrix value. A slight anisotropy of solid tortuosity is observed. The measurements carried out on our set of samples shows no clear influence of the pore size on the tortuosity.

Independent measurements show up that both poral space and solid matrix presents angular dependencies. A systematic study of transport properties dependence on parameters such as tortuosity and porosity as well as cells orientation distribution is undergoing using other samples of different textures.

Acknowledgments

The authors wish to thank Recemat Company for providing the samples, the ID19 beam team for helpful assistance at ESRF synchrotron facility, and the French government financial support in the frameworks of CNRS Energy program: PR Specimousse.

REFERENCES

1) M. F. Ashby, A. G. Evans, N. A. Fleck, L. J. Gibson, J. W. Hutchinson and H. N. G. Wadley: *Metal foams: A design guide Boston*, (MA, Butterworth, Heinemann, 2000).
2) J. Banhart: Progress in materials Science. **46** (2001) 529–532.
3) L. Tadrist, M. Miscevic, O. Rahli and F. Topin: Experimental Thermal and Fluid Science. **28** (2004) 193–199.
4) D. Sullines and K. Daryabeige: Proc. 35th AIAA Thermophysics Conference. Anaheim, CA, 2001.
5) K. Vafai and C. L. Tien: Int. J. Heat Mass Transfer. **25** (1982) 1183–1190.
6) S. Catillon, C. Louis, F. Topin, J. Vicente and R. Rouget: Proc. 2nd France-Deutchland Fuel Cells Conference. Belfort, France, 2004.
7) K. Boomsma and D. Poulikakos: International Journal of Heat and Mass Transfer **44** (2001) 827–836.
8) V. Bhattacharya, R. Calmidi and L. Mahajan: Int. J. Heat Mass Transfer. **45** (2002) 1017–1031.
9) A. F. Bastawros, A. G. Evans and H. A. Stone: Evaluation of cellular metal heat transfer media. 1998, Harvard University Report.
10) J. Vicente, J. V. Daurelle, F. Topin and L. Tadrist: Proc. 4th Int. Conf. on "Porous Metals and Metal Foaming Technology. Kyoto, Japan, 2005.
11) S. Catillon, C. Louis, F. Topin, J. Vicente and R. Rouget: Journal of Hydrogen Energy. (2005) In Press.
12) B. Zeghondy, J. Taine and E. Iacona: Proc. ASME International Mechanical Engineering Congress. 2004.
13) X. Badiche, S. Forest, T. Guibert, B. Y., P. Ienny and M. Croset: Materials Science and Engineering. **A289** (2000) 276–288.
14) F. Topin, J. P. Bonnet, J. Vicente and T. L.: Advanced material Engineering, (2006).
15) J. Vicente, F. Topin, J. V. Daurelle and F. Rigollet: Proc. 13th International Heat Transfer Conference. Sydney, 2006.
16) R. A. Drebin, L. Carpenter and P. Hanrahan: Proc. Computer Graphics, ACM Siggraph '88. 1988, 65–74.
17) S. Parker, M. Parker, Y. Livnat, P. Sloan, H. C. and P. Shirley: Proc. Viz. and Comp. Graph. 1999, 238–250.
18) T. McInerney and D. Terzopoulos: Medical Image Analysis. **1** (1996) 91–108.
19) W. E. Lorensen and H. E. Cline: Computer Graphics. **21** (1987) 163–169.
20) P. C. Carman: Trans. Instn Chem. Engrs. **15** (1937) 150–156.
21) P. M. Adler: Porous Media, geometry and transport. series in chemical engineering, ed. Butterworth-Heinemann, Butterworth/Heinemann, (1992).
22) J. A. Sethian and R. Kimmel: Proc. Nat. Acad. Sci. **95** (1988) 8431–8435.
23) J. A. Sethian: Level Set Methods and Fast Marching Methods. Cambridge, UK, Cambridge University Press, (1999).
24) T. Deschamps and L. D. Cohen: Medical Image Analysis. **5** (2001) 281–299.
25) J. F. Delerue, E. Perrier, Z. Yu and B. Velde: Physics and Chem. of the earth. **24** (1999) 639–644.
26) T. Dillard, F. N'Guyen, S. Forest, Y. Bienvenu, J.-D. Bartout, L. Salvo, R. Dendievel, E. Maire, P. Cloetens and C. Lantuéjoul: Proc. 3rd International Conference on Cellular Metals and Metal Foaming Technology (MetFoam 2003. Berlin (Germany), 2003, 301–306.
27) C. J. Pudney: Proc. CVIU. 1998, 404–413.
28) C. Lohou and G. Bertrand: Proc. DGCI. 2002, 102–113.
29) S. Decker, S. Möbbauer, D. T. Nemoda and T. Zapf: Proc. 6th int conf. on tech. and combustion for a clean environment. Port, Portugal, 2001.
30) H. L. Pan, O. Pickenacker, K. Pickenacker, D. Trimis, S. Möbbauer, K. Wawrzinek and T. Weber: 2002 [cited. Institute of Fluid Mechanics, University of Erlangen-Nuremberg Cauerstr. 4, D-91058 Erlangen, Germany.
31) R. A. Writz: Proc. the American Society of Mechanical Engineers National Heat Transfer Conference. Baltimore, MD, 1997.
32) A. F. Bastawros: Proc. Symposium on the Thermal Management of Electronics (IMECE). Anaheim, CA, 1998.
33) S. Y. Kim, J.-M. Koo and A. V. Kuznetsov: Numer. Heat Transfer. Part A: Appl **40** (2001) 21–36.
34) A. Bhattacharya, V. V. Calmidi and R. L. Mahajan: Int. J. Heat Mass Transfer. **45** (2002) 1017–1031.
35) V. V. Calmidi and R. L. Mahajan: J. Heat Transfer. **121** (1999) 466–471.
36) M. Fetoui, F. Albouchi, F. Rigollet, F. Topin, M. Sassi and S. Ben Nasrallah: Proc. Congrès de la SFT 04. Giens, France, 2004.